Aeroelastic Behaviour of a Morphing Wind Turbine Rotor in Varying Wind

David MacPhee[a], Asfaw Beyene[b]

[a] San Diego State University, San Diego, CA, USA, macphee@rohan.sdsu.edu
[b] San Diego State University, San Diego, CA, USA, abeyene@mail.sdsu.edu

Abstract:

Wind turbines are usually optimized at or near the mean wind velocity, having peak performance at the so-called design point. Unfortunately, away from this point, wind energy conversion efficiency can drop drastically, which can be problematic especially for sites with highly variable winds. Recent strategies have been adopted to mitigate these losses, most notably pitch control techniques, which effectively alter the local attack angles of the blades in order to more efficiently or safely handle external loadings. These strategies can be very costly, however, and thus are only employed where economically feasible. This study investigates, both experimentally and numerically, a flexible wind turbine rotor which can effectively alter its local attack angle without the use of an active control system. The flexible blades serve as a low cost, simplistic alternative to traditional pitch control schemes, and are tested in various wind speeds herein, with comparisons to a geometrically identical rigid blade. The results indicate that significant advantages are afforded by the flexible design, including increased torque coefficient and range of operability, both of which correspond to an increase in power generation over the rigid-bladed rotor.

Keywords:

Flexible, Wind, Energy, Conversion, FSI

1. Introduction

The aerodynamic design of Horizontal-Axis Wind Turbines (HAWTs) is fairly well established. Over the years, wind turbine designers have continued to optimize rotors and blades to the extent that at operational conditions, aerodynamic energy conversion efficiencies can be as high as 50% [1]. Due to the recent unprecedented demand for electricity from renewable sources, these turbines have increased dramatically in size in order to increase swept area and hence, energy capture. As a result, HAWTs have become much more economically viable, and capacity worldwide has skyrocketed in the recent past, from 31GW in 2002 to almost 283GW in 2012 [2].

Most of the larger HAWTs in use today employ some form of pitch control, wherein the attack angle of blades can be altered as a function of turbine rotational speed and upstream wind speeds, placing airfoil cross-sections in a more efficient position serving to enhance lift and mitigate drag. These control schemes, which are active in nature, serve three main purposes: 1) to increase efficiency at part-loading, offering an optimal attack angle as wind speed inevitably vary in time, 2) to maintain power output at or above rated speeds, and 3) to protect blades in damagingly high wind conditions. Pitch control schemes can be quite costly, though, and are usually only employed in larger turbines, where increased energy capture justifies upfront costs associated with their implementation.

For those turbines which do not implement pitch control, which represent a vast number of smaller HAWTs or installations in off-grid areas, the turbine is subject to significant declines in efficiency as operational conditions vary from the optimum. In areas where wind speed is highly variable, this can constitute a large percentage of operational time, and as a result energy conversion losses associated with this performance degradation can be substantial. Due to these problems, the overall conversion efficiency of many smaller HAWTs is greatly diminished as compared to their larger, more expensive counterparts. Due to the relatively low Reynolds numbers encountered by airfoil

cross-sections in smaller wind turbines, lift-to-drag ratios are decreased significantly [3], exacerbating the problem.

Due to the infeasibility of pitch control tactics in many HAWT installations, the purpose of this study is to investigate a low-cost simplistic pitch control mechanism, performing the same end results as active schemes but doing so passively, incorporating flexibility into the design process. This *morphing blade* design has the ability to adapt its geometry passively according to operational conditions, needing no costly control scheme and associated upfront installation costs. The impetus for this turbine design lies in the world of nature, a design strategy known as bio-mimicry.

Inspired by evolutionary design, bio-mimicry is the science of applying nature's solutions to engineering problems. Through millions of years of genetic optimization, natural systems have become incredibly efficient; as an example, dolphin locomotion has been estimated at 81% efficiency [4], while screw type propeller efficiencies vary from 28-65% [5]. Previous studies [6-9] have proven that the morphing turbine design can increase aerodynamic performance in part- and over-load conditions, delay airfoil stall, and act as a low-cost, passive pitch control device serving a similar purpose to active types but requiring no sensors, motors or control systems. Much as the dolphin augments its geometry to enhance swimming efficiency, the morphing turbine is able to change its geometry to allow for more efficient energy conversion.

Fluid-solid analysis of wind turbines remains a popular topic in engineering research (e.g., [10-11]), and the morphing blade has been studied by the authors previously, albeit in a two-dimensional setting [6-9]. However, this study incorporates both experimental and numerical findings into the behaviour of such a flexible turbine over several wind speeds, and is the first study of its kind known to the authors.

2. Mathematical Modelling

2.1. Fluid-Structure Interaction

Tasked with simulating both fluid and solid dynamics in a coupled fashion, the morphing HAWT simulation conducted herein is an example of a *multiphysics* phenomenon; that is, there are distinct governing equations for fluid and solid domains, and both must be resolved adequately to be considered accurate. The simulation here is built upon the OpenFOAM [12] framework, a finite-volume toolbox capable of such analysis, as it is capable of describing both fluid and solid motion and has dynamic mesh handling capabilities.

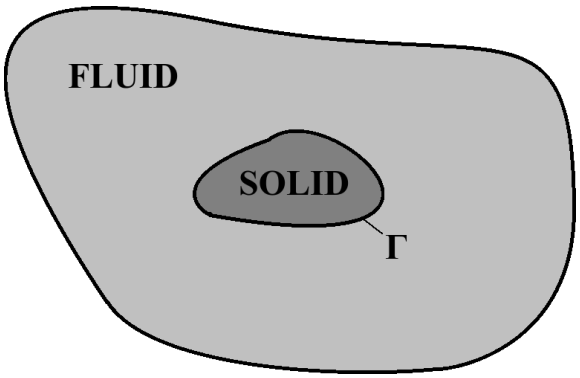

Figure 1: Outline of a typical fluid-structure problem, showing interface Γ.

The typical outline of a FSI boundary value problem is shown in Fig. 1, where the fluid is seen to occupy a volume distinct from that of the solid. Also shown is the interface boundary, Γ, and although not seen in Fig. 1, there exists also the possibility of other boundaries on the fluid and/or solid domains. The FSI algorithm used herein is an example of a strongly coupled, transient

segregated solver, meaning that solid and fluid domains are solved separately, and in succession, until a convergence tolerance is reached (to be discussed below) before time can be incremented and the solution can be progressed. An overview of the solution procedure for a single time step is shown in Fig. 2.

Since fluid and solid domains are separately treated, their mathematical descriptions are handled analogously below, after which a short discussion on the mesh motion algorithm, domain coupling and convergence criteria are presented.

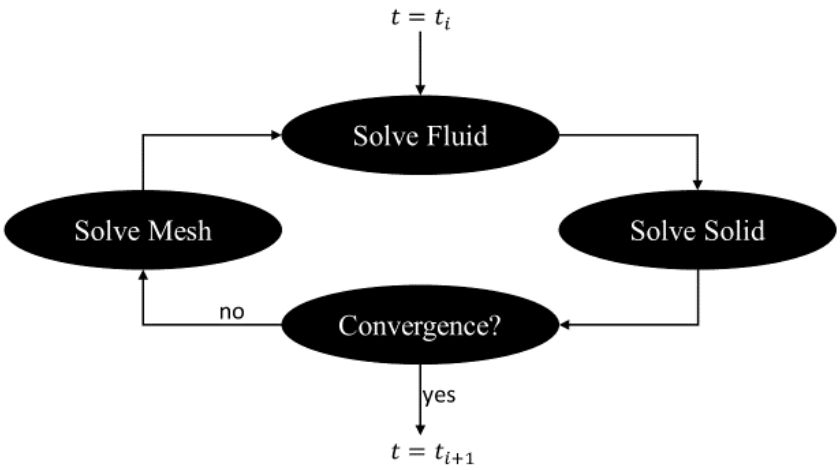

Figure 2: FSI solution procedure.

2.2. Fluid Domain

The equations of motion for the fluid domain consist of the Navier Stokes equations for Reynolds averaged (mean) flow, for which the mass and momentum equations must be cast in the arbitrary Lagrangian-Eulerian formulation in order to allow for mesh motion:

$$\nabla \cdot \left(\mathbf{u} - \hat{\mathbf{u}} \right) = 0 \tag{1}$$

$$\rho \left[\frac{d\mathbf{u}}{dt} + \left(\mathbf{u} - \hat{\mathbf{u}} \right) \cdot \nabla \mathbf{u} \right] = -\nabla p + \nabla \cdot \left[2\mu \mathbf{S} + \boldsymbol{\tau} \right] + \rho \mathbf{f} \tag{2}$$

Here, the pressure and velocity fields, p and $\mathbf{u}$, respectively, are time-averaged, and the mesh velocity is denoted by $\hat{\mathbf{u}}$. The mean rate of strain tensor is $\mathbf{S}$ and $\boldsymbol{\tau}$ denotes the Reynods stress tensor. In this study, the equations of motion are solved in a rotating reference frame, so the body force $\mathbf{f}$ must incorporate both the Coriolis and centrifugal forces:

$$\mathbf{f} = -2\boldsymbol{\Omega} \times \mathbf{u} - \boldsymbol{\Omega} \times \left(\boldsymbol{\Omega} \times \mathbf{r} \right) \tag{3}$$

Here, $\mathbf{r}$ is the position vector, and the turbine is assumed to rotate at angular velocity $\boldsymbol{\Omega}$ along an axis coincident with the origin. To resolve the Reynolds stress, the solver makes use of the k-ω-SST turbulence model [13], often used for wind turbine applications as it performs well inside and outside of boundary layers. The PISO algorithm is used with a time step sized based on the local Courant number (Co), such that the maximal Co in the fluid domain remains less than one. Finally, the temporal discretization is completed using the standard implicit Euler technique.

2.3. Solid Domain

The solid domain governing equations, much like the fluid, involve mass and linear momentum conservation and are written as:

$$\frac{D\rho}{Dt} = 0 \tag{4}$$

$$\frac{D}{Dt}(\rho\mathbf{u}) = \nabla\cdot\boldsymbol{\sigma} + \rho\mathbf{f} \tag{5}$$

However, as the fluid domain assumption of incompressibility does not apply here, the gravitational force **g** must also be accounted for when applying the body force:

$$\mathbf{f} = -2\boldsymbol{\Omega}\times\mathbf{u} - \boldsymbol{\Omega}\times(\boldsymbol{\Omega}\times\mathbf{r}) + \mathbf{g} \tag{6}$$

The solid model herein allows for nonlinear deflections and assumes a linear elastic isotropic (St. Venant-Kirchhoff) material, which relates the Cauchy stress $\boldsymbol{\sigma}$ to the 2nd Piola-Kirchhoff stress $\boldsymbol{\Sigma}$ as:

$$\boldsymbol{\sigma} = J^{-1}\mathbf{F}\,\boldsymbol{\Sigma}\,\mathbf{F} \tag{7}$$

Here, **F** is the deformation gradient tensor, and *J* its determinant. The material constitutive relationship between stress and Lagrangian (Green) strain tensor **E** is as follows:

$$\boldsymbol{\Sigma} = 2G\,\mathbf{E} + \lambda\,\mathbf{I}\,\mathrm{tr}(\mathbf{E}) \tag{8}$$

where Lamé's parameters, *G* and λ, are usually described in terms of the Poisson ratio ν and Young's modulus E:

$$\lambda = \frac{\nu\mathrm{E}}{(1+\nu)(1-\nu)}, \quad G = \frac{\mathrm{E}}{2(1+\nu)} \tag{9}$$

The system of equations is subsequently solved using the updated Lagrangian approach [14], wherein the reference configuration is treated as the material reference frame and the solid mesh, as well as the total stress and strain tensors are updated each time step.

2.4. Mesh Domain

In order to allow for solid boundary motion, the fluid domain must move to accommodate this motion. The motion is handled by solving a Laplacian equation with variable diffusivity:

$$\phi\nabla^2\hat{\mathbf{d}} = 0 \tag{10}$$

where the mesh displacement each time step is $\hat{\mathbf{d}}$ and the diffusivity varies according to the distance from the nearest FSI boundary, *y*:

$$\phi = \frac{1}{y^2} \tag{11}$$

This formulation ensures adequate cell density is retained near regions of interest (boundary layers) and avoids skewed volumes which can lead to inaccuracy or instability of the model.

2.5. Coupling and Convergence

Coupling is achieved via the equivalence of traction forces on both solid and fluid side of the interface:

$$(\boldsymbol{\sigma}\cdot\mathbf{n})_{fluid,\Gamma} = (\boldsymbol{\sigma}\cdot\mathbf{n})_{solid,\Gamma} \tag{12}$$

where the Cauchy stress tensor in the fluid is evaluated from the pressure and velocity gradients available during solution progression in the fluid, and are applied to the solid using a fixed normal derivative Neumann boundary condition on the updated displacement variable [14].

Each iteration, the interface displacement, calculated with the solid solver, is relaxed using Aitken's delta-squared process. Convergence is then said to be achieved if the sum of all relaxed nodal displacement magnitudes is less than 0.1% of that predicted on the first iteration step, where

simple fixed relaxation was conducted. This value provided a good balance between accuracy and tractability and was used in all simulations herein. Most time steps required 7-10 sub-iterations of the FSI solver.

3. Experimental Methods

Two sets of rotor blades were constructed for experimental consideration. Each set was designed to integrate seamlessly to the hub piece, seen in Fig. 3, and allowed for variable blade pitch angles as well as blade interchangeability. The blades themselves were constructed of poured polyurethane and cast into acrylic moulds.

Figure 3: Experimental apparatus, showing turbine in test position.

The rigid blades were fabricated using a single pouring process and were constructed of a light polyurethane foam which provided an adequate amount of structural integrity without unnecessary weight. The process for manufacturing the flexible blades was much more involved, and required a two-part moulding process, wherein the inner blade support was first cast using a different set of acrylic moulds. After casting this inner "spine" portion, seen as the darker region in Fig. 4, it was then placed into the first set of moulds in which the flexible material was poured around, ensuring an identical geometry (at zero load conditions) to the rigid blade design.

The blade itself has a NACA 0015 cross-section, with chord length 12.0cm at L_2 "Level-2" and 6.0cm at L_1, Fig. 4. The exact placement of the rigid support within the flexible material is described in Fig. 5. Note that the blades are designed to be symmetric, and due to the design of the hub they can be placed with variable pitch angle.

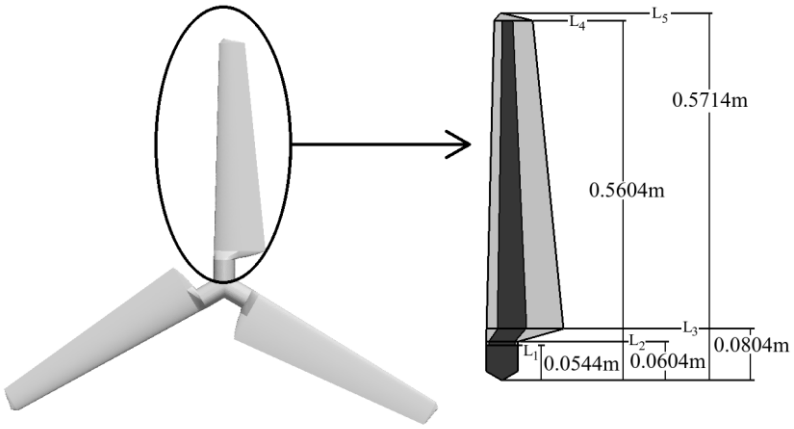

Figure 4: Description of flexible rotor, showing flexible and rigid (dark grey) portions.

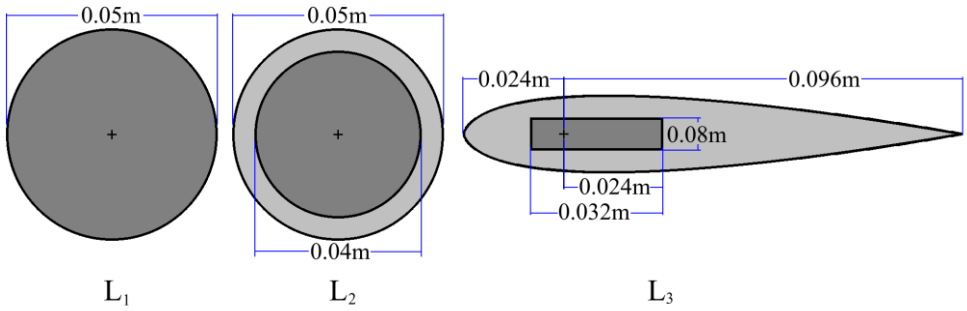

Figure 5: Cross-sectional distribution of flexible material (grey) and rigid (dark grey)

Both rotors were then tested in a novel, large diameter wind tunnel specifically designed for experiments with small wind turbines. With a diameter of over 1.5m, this apparatus includes flow straighteners, a large duct fan equipped with a variable frequency drive, and adequate equipment to ensure proper recording of torque, angular velocity, air velocity, humidity, temperature and pressure data, used in rotor performance calculations.

3.1. Experimental Results

The performance of wind turbines is usually evaluated using the power coefficient C_P:

$$C_P = \frac{P}{P_{wind}} \tag{13}$$

where P is the power developed in the turbine and P_{wind} is the power available in the wind. However, in the present case study, there are significant blockage effects which artificially raise the performance, in some cases to levels exceeding the Betz limit of 0.593. Reasons for this are due to the proximity of wind tunnel walls, forcing more air through the turbine than would be otherwise possible. Whereas open turbines impart radial momentum onto freestream air this is substantially reduced in the present study. Therefore, comparisons between rotor types will be conducted using only the torque coefficient, T^* [15]:

$$T^* = \frac{1}{TSR}\left(\frac{2T\Omega}{\rho V^3 \pi R^2}\right) \tag{14}$$

where TSR is the Tip-Speed Ratio, defined as the ratio of the blade tip velocity to the freestream velocity:

$$TSR = \frac{\Omega R}{V} \tag{15}$$

All rotor blades were then attached to the hub, using a blade pitch angle of 6°, and tested from cut-in to cut-out speed in increments of around 50 rpm. The resulting torque coefficients measured for the rigid and flexible blades can be seen in Figs. 6-8 for wind speeds of 2.05, 2.60 and 3.15 m/s, respectively.

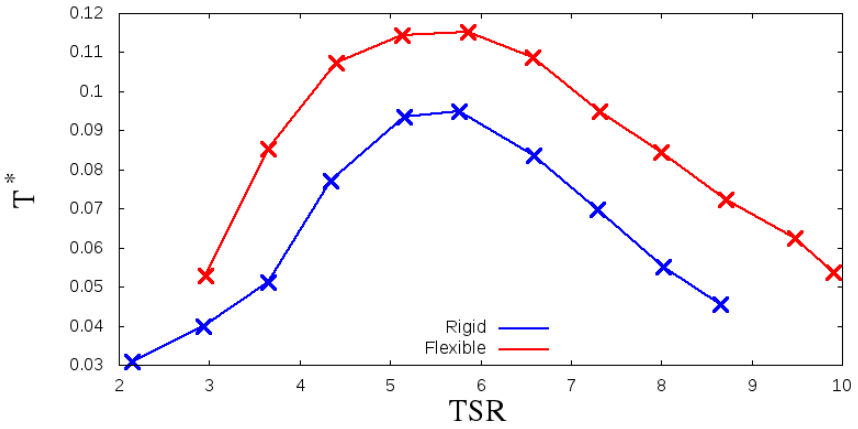

Fig 6: Experimental torque coefficients, freestream velocity of 2.05 m/s.

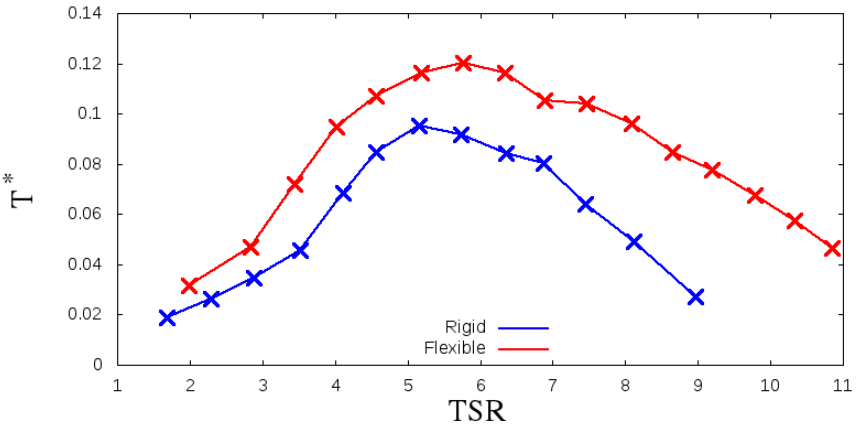

Fig 7: Experimental torque coefficients, freestream velocity of 2.60 m/s.

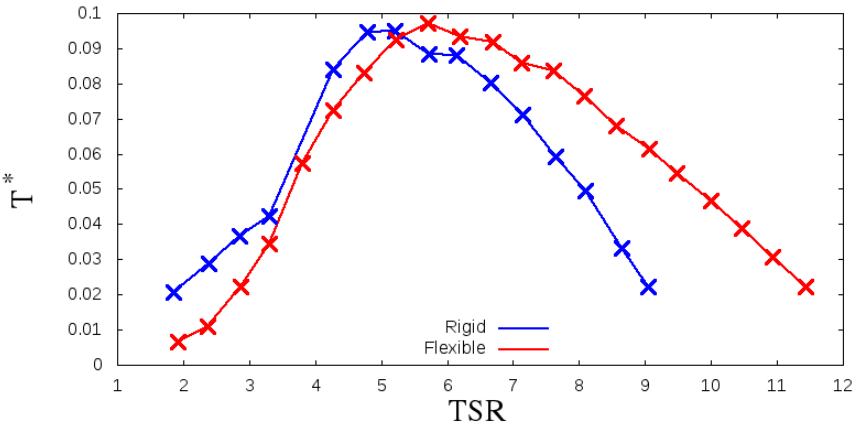

Fig 8: Experimental torque coefficients, freestream velocity of 3.15 m/s.

It is clear, looking at Figs. 6-8, that the torque coefficients for the flexible blade are significantly higher, especially so for lower wind speeds and higher tip-speed ratios. To illustrate these differences, we take the area under each curve and let this value equal χ, which should serve as a good indicator of the differences in energy capture through utilization of each blade type:

$$\chi = \int T^* \, dTSR \tag{16}$$

Through evaluation of χ, it was found that the area under the curve was **43.5% higher** for the wind speed of 2.05 m/s**, 74.2% higher** for the wind speed of 2.60 m/s, and **27.16% higher** for the wind speed of 3.15 m/s. In other words, the flexible blade proved far superior in all cases to the rigid one, due to its ability to augment its geometry, placing blades in a more advantageous position in varying winds.

Looking at Figs. 6-8, it is clear that the gains observed through the implementation of the morphing blades diminished somewhat with increasing velocity. At the lowest wind speed tested, Fig. 6, the morphing blade design is clearly superior throughout. The curves tend to be somewhat closer for the median wind speed, and approach similar maximal torque coefficients for the maximum wind speed. It can also be deduced that *operational envelope*, that is, the difference between highest and lowest registered tip-speed ratios, is increased for increasing wind speed.

These performance improvements can be attributed to the dynamic nature of the morphing blade design. Whereas the three non-dimensional rigid-blade torque curves coalesce into very similar profiles, the morphing blade geometry changes according to the aerodynamic forces acting upon it, and as a result very different torque curves are realized. Furthermore, as wind speed increases, airfoil attack angles become higher in general, with increased incidence of blade stall. Due to this fact, separation is expected to occur for much of the lower part of the blade, and for much of the operational envelope, in Fig. 8, meaning that little can be gained with slight modifications of the camber line due to morphing. When tip-speed ratios reach a certain point and boundary layers are expected to re-attach for much of these areas, the morphing blade is seen to exhibit superior performance, as seen in the right hand side of Fig. 8.

To provide further insights into how the morphing blade achieves this superior performance, the results of the FSI solver are presented in the following section.

4. Simulation Results

For all simulations, it should be noted that to decrease the amount of computational time required, the following simplifications were made: 1) the solid domain was first initialized to a steady-state solution applying only the centrifugal forces, and 2) only the back half of the blade is considered, due to the presence of the inner spine which prevents bending in the leading edge of the blade. These strategies drastically reduced the amount of computational time required and aided in solver stability without sacrificing accuracy.

The fluid domain was meshed using gmsh [16], an open-source, unstructured tetrahedral mesh generating tool. Conversely, the solid mesh was created using the native OpenFOAM meshing tool, blockMesh. After considerable mesh sensitivity tests, including domain entrance and exit length independence, were completed for both domains [17], a grid size of 339k cells and 16k cells were utilized for the solid and fluid domains, respectively.

The test case of V = 2.60 m/s, and an angular velocity of 300rpm (31.416 rad/s) is chosen for simulation. This corresponds to a *TSR* of around 6.8, just past the optimum T^* found for both rigid and flexible blades in Fig. 7. For the rigid-bladed simulation, the FSI loop and solid solver portions of the code were commented out, and the algorithm was run in serial, requiring a few days to come to a steady state solution, which occurred at around the 5^{th} rotor revolution. The simulated rotor torque for the rigid blade was 0.1614 Nm, which agrees with the measured (experimental) value of 0.159 to within 1.5%.

For the flexible test, the velocity and pressure fields in the fluid were initialized using the saved values from the rigid-bladed simulation, which acted to further reduce the computational time required. Nevertheless, the simulation still required 2.0 revolutions until a steady torque was realized, which required just over 32 days of CPU time as the simulation was also run in serial. The simulated torque for this case was calculated to be 0.196 Nm, which agreed to within 6.2% of the experimental value of 0.209 Nm. From this and the rigid-bladed simulation, the FSI algorithm can thus be considered validated through comparisons to experimental data.

The reasons for increased torque, and hence, increased energy conversion are due to the morphing blades' ability to bend towards the flow direction when the airfoil is placed in a disadvantageous position. Fig. 9 shows the displacement magnitude of the rotor during simulation, where it is clearly seen that the blades act to bend towards flow, reaching a maximal value somewhere near mid-radius, and returning to a smaller displacement at the blade tips.

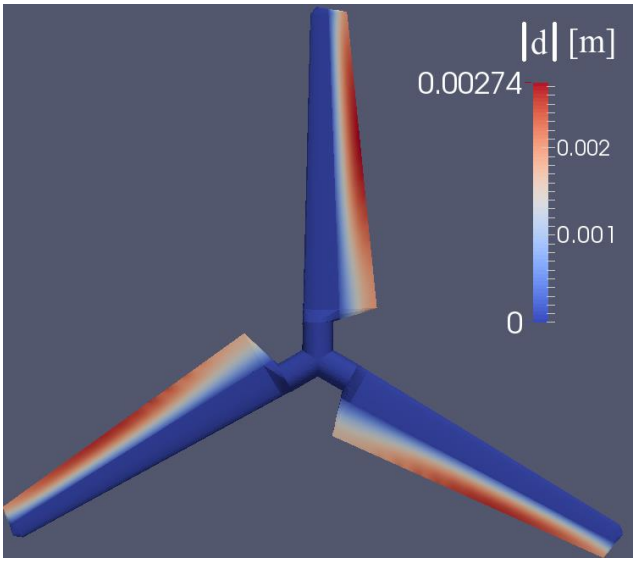

Figure 9: Displacement magnitude distribution during FSi simulation.

It is well-known that one very important parameter regarding airfoil performance is the lift-to-drag ratio. For the chordal Reynolds numbers experienced herein, which vary between 29,000 at the blade root and 73,000 at its tip, the maximal lift-to-drag ratio occurs somewhere between 5-7°. Performing simple calculations regarding the local attack angle of the blades, one can find that the location at which optimal attack angle occurs, assuming 6°, is at a radius of around 0.39m. Looking at Fig. 9, this is very near the location where maximal deflection is occurring – suggesting that at all radii, the flexible nature of the blade is adapting its chord-wise deflection towards the optimum angle of around 6°. This information is corroborated in Fig. 10, where trailing edge tip deflection magnitude is seen to increase until the location of optimal rigid bladed attack angle, and decrease afterwards. This action effectively changes the cross-section of the blade from a symmetric to a varying, cambered airfoil at all locations.

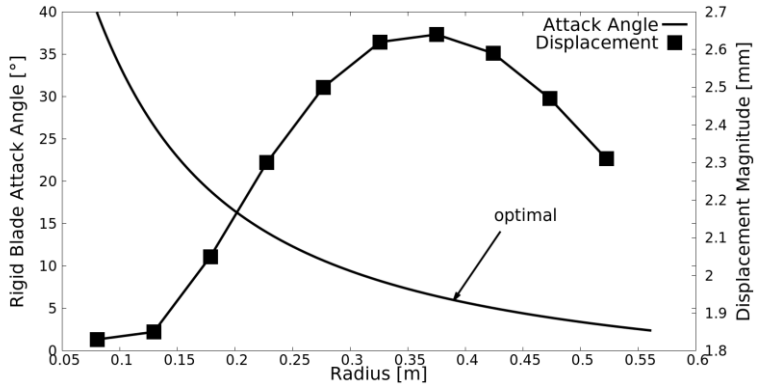

Fig. 10: Rigid-bladed attack angle as a function of blade radius, showing optimum (6°) location, plotted alongside the trailing edge displacement magnitude of the flexible blade.

Unfortunately, due to the nature of the blade construction, deflection is hindered near the hub, where the greatest increases in aerodynamic performance could be attained. This is an unavoidable consequence of the symmetric blade designed herein for proof-of concept. Unfortunately, due to the nature of the blade construction, deflection is limited near the hub, where the greatest increases in aerodynamic performance could be attained. This is an unavoidable consequence of the symmetric blade designed herein for proof-of concept.

In summary, the morphing turbine blade design is able to adapt its geometry, which should be especially effective in varying winds as well as over and part-loading scenarios. Through passive deflection of its geometry, the blades are able to effectively alter their attack angles to position itself in a more efficient position, effectively acting as a pitch-control device. This morphing mechanism which is passive in nature, could be a simplistic, low cost addition to HAWTs, and should greatly benefit those turbines which otherwise cannot afford active pitch control strategies.

5. Conclusions

This study investigated both experimentally and numerically the behaviour of a flexible or morphing blade wind turbine for use in wind energy conversion. The flexible blades were constructed to be geometrically identical to the rigid ones at zero load, and were tested in a large diameter wind tunnel at wind speeds of 2.05, 2.60 and 3.15 m/s. The following conclusions can be made from this study:

- In all three wind speeds, the torque coefficients proved to be much higher for the flexible blade in the majority of tip-speed ratios. Moreover, the cut-out turbine speed increased in all three cases.
- Taking the area under the performance curve, which should translate directly to energy conversion, the flexible blade far outperformed the rigid one. In fact, up to a 74.2% increase in this parameter was recorded for the median wind speed;
- The finite-volume FSI solver developed herein accurately predicted torque for both the rigid and flexible blades in a given freestream velocity and tip-speed ratio. From viewing post-processing images, it is obvious that the increase in performance comes from the flexible bladed design's ability to change its attack angle in response to external loadings from wind.

In essence, this analysis of the morphing HAWT rotor in varying wind regimes has shown that increases in efficiency would likely be found in a wide range of operational conditions. The morphing design should prove especially useful for cases where pitch control strategies are not economically feasible, providing an increase in operational envelope as well as a boost in efficiency at part and over- load conditions.

Nomenclature

Latin Characters

C_P	Power coefficient, (-)
d	Displacement, m
E	Green-Lagrangian strain tensor, (-)
E	Young's modulus, kg/(m s^2)
F	Deformation gradient tensor, (-)
f	Volume-weighted body force, m/s^3
g	Gravitational acceleration, m/s^3
G	Lamé's second parameter, kg/(m s^2)
I	Identity tensor, (-)
J	Jacobian determinant, (-)
n	Outward facing unit normal, m
p	Thermodynamic pressure, kg/(m s^2)
P	Power, kg m^2/s^3
R	Blade radius, m
S	Mean rate of strain tensor (1/s)
t	Time, s
T	Torque, Nm
T^*	Torque coefficient, (-)
u	Continuum velocity, m/s
$\hat{\mathbf{u}}$	Mesh velocity, m/s
V	Freestream velocity, m/s
y	Distance to nearest FSI boundary, m

Greek symbols

Γ	FSI boundary, (-)
λ	Lamé's first parameter, kg/(m s^2)
μ	Dynamic viscosity, kg/(m s)
ν	Poisson's ratio, (-)
ρ	Density, kg/m^3
σ	Cauchy stress tensor, kg/(m s^2)
Σ	Second Piola-Kirchhoff stress tensor, kg/(m s^2)
$\boldsymbol{\tau}$	Reynolds stress tensor, kg/(m s^2)
φ	Variable diffusivity, m^2
χ	Total torque coefficient integral, (-)
Ω	Rotational velocity, (1/s)

Acronyms

Co	Courant number

HAWT	Horizontal Axis Wind Turbine
PISO	Pressure-Implicit with Splitting of Operator
TSR	Tip-Speed Ratio

References

[1] G. M. J. Herbert, S. Iniyan, E. Sreevalsan, and S. Rajapandian. A review of wind energy technologies. Renewable and Sustainable Energy Reviews, 11:1117–1145, 2007.

[2] Global Wind Energy Council. Global wind statistics 2012. 2012.

[3] Lissaman, P. B. S., 1983. Low-Reynolds-number airfoils. Annual Review of Fluid Mechanics 15.1: 223-239.

[4] Fish F., 1993. Power output and propulsive efficiency of swimming bottlenose dolphins. J. Exp. Biol. 185:179–193.

[5] J. B. Brandt and M. S. Selig, 2011. "Propeller performance data at low Reynolds numbers". In 49th Annual AIAA Aerospace Sciences Meeting.

[6] D. MacPhee and A. Beyene. Fluid-structure interaction of a morphing symmetrical wind turbine blade subjected to variable load. International Journal of Energy Research, 37(1):69–79, 2013.

[7] MacPhee, D. and Beyene, A., 2011. A flexible turbine blade for passive blade pitch control in wind turbines. IEEE Power Engineering and Automation Conference 2011. Wuhan, China, 8-9 September 2011. doi: 10.1109/PEAM.2011.6134834.

[8] Krawczyk, P., Beyene, A. and MacPhee, D., 2012. Fluid-structure interaction of a morphed wind turbine blade, International Journal of Energy Research 37(14), 1784-1793.

[9] Beyene, A., & Peffley, J. (2009). Constructal theory, adaptive motion, and their theoretical application to low-speed turbine design. Journal of Energy Engineering, 135(4), 112-118.

[10] Y. Bazilevs, M-C. Hsu, I. Akkerman, S. Wright, K. Takizawa, B. Henicke, T. Spielman, and T. E. Tezduyar. 3d simulation of wind turbine rotors at full scale. part i: geometry modeling and aerodynamics. International Journal for Numerical Methods in Fluids, 65(1–3):207–235, 2011.

[11] Y. Bazilevs, M-C. Hsu, J. Kiendl, R. Wchner, and K. Bletzinger. 3d simulation of wind turbine rotors at full scale. part ii: fluidstructure interaction modeling with composite blades. International Journal for Numerical Methods in Fluids, 65(1–3):236–253, 2011.

[12] OpenCFD Ltd. OpenFOAM - the open source computational fluid dynamics toolbox. http://www.openfoam.org, 2015.

[13] F. R. Menter. Zonal two equation k-ω turbulence models for aerodynamic flows. AIAA Paper, 1993.

[14] Z. Tukovic and H. Jasak. Updated lagrangian finite volume solver for large deformation dynamnic response of elastic body. Transaction of Famena, 2007.

[15] Chaitep, S., Watanawanyoo, P., & Hirahara, H. (2011). Performance Evaluation of Curved Blades Vertical Axis Wind Turbine. European Journal of Scientific Research, (57), 435-446.

[16] C. Geuzaine and J. F. Remacle. Gmsh: a three-dimensional finite element mesh generator with built-in pre- and post-processing facilities. International Journal for Numerical Methods in Engineering, 79(11):1309–1331, 2009.

[17] David MacPhee. Flexible Blade Design for Wind Energy Conversion Devices. PhD Thesis, University of California, San Diego, 2014